Acta Biochim Biophys Sin 2026, 58(5): 1069–1082
https://cstr.cn/32197.14.abbs.2025163
https://doi.org/10.3724/abbs.2025163
Original Article

Original Article

Myocyte enhancer factor 2A orchestrates vascular redox homeostasis via direct transcriptional activation of SIRT1

Benrong Liu[1,†,*], Lei Fang[1,†], Chunxia Miao[1,†], Xinyu Wen[1], Xiumiao Zheng[1], Minxing Xu[1], Junli Lin[1], Yujuan Xiong[2], and Shi-Ming Liu[1,*]

[1]Department of Cardiology, Guangzhou Institute of Cardiovascular Disease, Guangdong Key Laboratory of Vascular Diseases, State Key Laboratory of Respiratory Disease, the Second Affiliated Hospital, Guangzhou Medical University, Guangzhou 510260, China, and [2]Department of Laboratory Medicine, Panyu Hospital, Guangzhou University of Chinese Medicine, Guangzhou 511400, China

[†]These authors contributed equally to this work.

*Correspondence address. E-mail: liubenrong@gzhmu.edu.cn (B.L.); liushiming@gzhmu.edu.cn (S.L.)

Received 21 April 2025 Accepted 4 August 2025 Published 3 December 2025

Abstract

Myocyte enhancer factor 2A (MEF2A), a transcription factor implicated in coronary artery disease, remains unexplored in vascular redox regulation. To address this gap and overcome the limitations of current antioxidant therapies, we investigate the role of MEF2A in oxidative defense via human umbilical vein endothelial cells (HUVECs) and murine models. Adenoviral vectors encoding MEF2A-specific shRNAs or mRNAs are used to silence or overexpress *MEF2A* in HUVECs. For *in vivo* validation, endothelial-targeted *MEF2A* knockdown is achieved via AAV1-shRNA delivery in mice fed with a high-fat diet. Systemic redox status is assessed by measuring reactive oxygen species (ROS), glutathione homeostasis (GSH/GSSG ratio), the NADH/NAD^+ balance, the mitochondrial membrane potential ($\Delta\Psi m$), and 8-hydroxy-2′-deoxyguanosine (8-OHdG). Mechanistic insights are derived from immunofluorescence, qPCR, western blotting, and dual-luciferase reporter assays. *MEF2A* silencing induces redox imbalance, characterized by elevated ROS, a reduced GSH/GSSG ratio, and $\Delta\Psi m$ collapse. Conversely, MEF2A overexpression synergizes with SIRT1 to restore the glutathione pool, maintain NAD^+ homeostasis, and suppress ROS under oxidative stress. Chromatin immunoprecipitation confirms that MEF2A directly binds to two cis-elements in the *SIRT1* promoter, driving transcriptional activation. *In vivo*, MEF2A-deficient mice present increased vascular oxidative damage, as indicated by elevated DNA damage marker (8-OHdG) and ROS levels. The downregulation of SIRT1/PGC-1α in *MEF2A*-silenced cells is verified *in vivo*. Our findings establish MEF2A as a master regulator of endothelial redox defense via the SIRT1-PGC-1α axis, providing a mechanistic foundation for the treatment of oxidative cardiovascular disorders. This work suggests that pharmacological MEF2A activation is a novel strategy for precision antioxidant therapy in vascular medicine.

Key words oxidative stress, MEF2A, redox homeostasis, GSH/GSSG ratio, cardiovascular disease, NADH/NAD^+ ratio

Introduction

Oxidative stress is a pathophysiological state characterized by excessive reactive oxygen species (ROS) production overwhelming endogenous antioxidant defenses, and serves as a critical driver of cellular dysfunction and tissue damage in chronic diseases [1]. In the cardiovascular system, this redox imbalance triggers endothelial injury, initiating a cascade of events that culminate in atherosclerosis, hypertension, and ischemic heart disease [2–5]. While ROS are essential signaling molecules at physiological levels, their pathological accumulation induces DNA damage, lipid peroxidation, and mitochondrial impairment, with vascular endothelial cells being particularly vulnerable due to their direct exposure to hemodynamic stressors [6,7].

Vascular endothelial cells, far beyond their traditional role as passive blood vessel linings, function as dynamic biosensors that regulate vascular tone, thromboresistance, and inflammatory responses through paracrine signaling [8]. Emerging evidence positions endothelial redox dysregulation as the “first domino” in

© The Author(s) 2025. This is an open access article distributed under the terms of the Creative Commons Attribution-NonCommercial-NoDerivs License (https://creativecommons.org/licenses/by-nc-nd/4.0/).

atherosclerosis development, where the oxidative inactivation of nitric oxide synergizes with oxidized LDL uptake to drive foam cell formation and plaque progression [8–10]. Despite advances in antioxidant therapies (*e.g.*, vitamins, probucol and related phenols), clinical translation remains hampered by systemic toxicity and the inability to target endothelial-specific pathways [11]. This therapeutic gap underscores the urgency of identifying master transcriptional regulators of endothelial redox homeostasis.

Sirtuin 1 (SIRT1), an NAD^+-dependent deacetylase, and peroxisome proliferator-activated receptor γ coactivator-1α (PGC-1α), a master regulator of mitochondrial biogenesis, form a critical nexus for redox defense [12]. SIRT1 deacetylates PGC-1α to enhance mitochondrial function and ROS scavenging [13]. Pharmacological activators such as resveratrol improve vascular function [14]; however, their reliance on upstream transcriptional control mechanisms remains unexplored. This gap parallels broader failures of nonspecific antioxidants, highlighting the urgency of defining transcription factors that coordinate mitochondrial quality control and endogenous defenses.

Myocyte enhancer factor 2A (MEF2A), a member of the MADS-box transcription factor family, has emerged as a paradoxical player in cardiovascular biology [15–17]. MEF2A was originally identified for its essential role in muscle development through its regulation of myocyte differentiation and morphogenesis [18], and it has since been shown to perform pleiotropic functions across tissues. In immune regulation, a study by Renato Ostuni's group [19] revealed that PGE2 signaling in macrophages functionally inactivates MEF2A to modulate inflammatory gene expression, demonstrating its context-dependent role in immune modulation. In developmental biology, MEF2A regulates cell differentiation in *Dictyostelium discoideum*, where *mef2A*-deficient strains exhibit impaired prespore cell formation and spore production, highlighting its evolutionary conservation in cell fate determination [20]. Emerging evidence also links MEF2A to metabolic regulation, with studies showing its role in promoting CM proliferation through SphK2/S1P signaling, thereby extending the cardiac regenerative window [21]. Conversely, in cancer biology, MEF2A is overexpressed in colorectal cancer, where it activates WNT/β-catenin signaling to drive tumor proliferation, whereas metformin inhibits its oncogenic activity by promoting ubiquitin-mediated degradation [15]. Neurodegenerative disease research has further revealed the involvement of MEF2A in the regulation of autophagy [22]; its downregulation via enhancer methylation is correlated with impaired autophagic flux in Alzheimer's disease models [23]. These multifaceted roles collectively position MEF2A as a central node integrating developmental, metabolic, and stress-responsive signaling pathways.

While human genetic studies link MEF2A mutations to premature coronary artery disease [24,25] and dilated cardiomyopathy [26], its mechanistic role in vascular redox regulation remains enigmatic. Our previous work revealed the capacity of MEF2A to delay H_2O_2-induced endothelial senescence via PI3K/Akt/SIRT1 signaling [27] and mediate the vasculoprotective effects of resveratrol [22]. These findings suggest that MEF2A has potential as a redox-sensitive transcription factor, yet key questions remain. Does MEF2A directly orchestrate antioxidant gene networks? What molecular effectors execute their protective functions?

Here, we bridge this knowledge gap by delineating a novel MEF2A-SIRT1-PGC-1α axis essential for endothelial redox homeostasis. Through integrated *in vitro* and *in vivo* approaches, we demonstrated that (1) MEF2A deficiency precipitates mitochondrial ROS overflow and glutathione depletion via SIRT1 suppression; (2) MEF2A directly transactivates SIRT1 through conserved promoter elements, establishing a self-reinforcing antioxidant loop; and (3) endothelial-specific *MEF2A* knockdown in mice recapitulates human atherosclerotic phenotypes, including oxidative DNA damage and PGC-1α downregulation. Our findings not only redefine MEF2A as a transcriptional guardian of vascular redox equilibrium but also provide a mechanistic blueprint for developing precision therapies targeting this axis in cardiovascular diseases.

Materials and Methods

Cell culture

Primary human umbilical vein endothelial cells (HUVECs) were isolated from human umbilical cord veins (from Obstetrics Department of the Second Affiliated Hospital of Guangzhou Medical University) via a combination of trypsin-collagenase digestion and the differential adhesion method, followed by selection via endothelial cell culture medium (EBM-2; Lonza, Basel, Switzerland). HUVECs were maintained in EBM-2 basal medium (CC3156; Lonza) supplemented with 3% fetal bovine serum (FBS; Lonza), endothelial cell growth supplement (CC4176; Lonza), and antibiotics and incubated at 37°C in a humidified 5% CO_2 atmosphere. The isolation protocol was approved by the Ethics Committee of the Second Affiliated Hospital of Guangzhou Medical University (approval No. 2021-LCYJ-ZF-06).

Oxidative stress cell model

HUVECs were seeded in 48-well or 96-well plates and allowed to adhere overnight. The culture medium was then replaced by fresh complete medium containing a gradient of hydrogen peroxide (H_2O_2; 0, 50, 100, 200, or 400 μM). The cells were exposed to H_2O_2 for 1, 2, or 4 h, after which the treatment medium was aspirated and replaced by fresh medium. Following an additional 24-h incubation under standard culture conditions, cell viability was quantified. The exposure parameters yielding approximately 60% viability (200 μM H_2O_2 for 2 h) were selected to establish the oxidative stress model for subsequent experiments.

Assessment of cell viability

Cell viability was evaluated using the Cell Counting Kit-8 (CCK8; APExBIO Technology LLC, Houston, USA) following the protocols provided by the manufacturer. In brief, the existing cell culture medium was exchanged for fresh serum-free EBM-2 medium. Subsequently, 10 μL of CCK8 solution was introduced into each well containing 100 μL of medium and mixed gently. The plates were then incubated at 37°C in a 5% CO_2 atmosphere for 3–4 h. Absorbance was measured at a wavelength of 450 nm using a spectrophotometer.

Silencing or overexpression of *MEF2A in vitro*

Adenoviral expression vectors containing MEF2A/SIRT1-specific short hairpin RNA (shRNA) or overexpression cassettes were constructed. The mature shRNA sequences of MEF2A, SIRT1 shRNA, and NC were 5′-GGGCAGUUAUCUCAGGGUU-3′, 5′-GGCGGCUUGAUGGUAAUCAGUA-3′, and 5′-TAGTGAAGCCACAGATGTA-3′, respectively. A green fluorescent protein (GFP) reporter was incorporated downstream of target genes for expression monitoring. Viral packaging, purification, and titer determination

were performed by Shandong Weizhen Biosciences (Jinan, China). Control groups received miR-30-shRNA (5′-TAGTGAAGCCACAG ATGTA-3′) or GFP-expressing adenoviruses (Shandong Weizhen Biosciences). The transduction efficiency was verified via a fluorescence microscope (EVOS M7000; Thermo Fisher Scientific, Waltham, USA) prior to functional assays.

Assessment of the GSH/GSSG ratio

The glutathione redox status was determined via a commercial GSH/GSSG Assay Kit (S0053; Beyotime, Shanghai, China) according to the manufacturer's protocols. Samples from cells, plasma, and vascular tissues were processed in parallel.

Detection of cellular and mitochondrial ROS

Intracellular ROS were quantified via dihydroethidium (DHE; S0063; Beyotime). The cells were washed with PBS (37°C), incubated with 5 μM DHE in serum-free medium for 30 min in the dark, and then counterstained with Hoechst 33342 (Invitrogen, Waltham, USA) for 10 min, followed by taking photos under the EVOS M7000 fluorescence microscope. The fluorescence intensity (Ex/Em: 535/610 nm) was quantified via ImageJ.

Mitochondrial ROS were assessed via BBcellProbe® OM08 (BB-46091; Bestbio, Nanjing, China). The cells were incubated with a 1:100-diluted probe in HBSS (Bestbio, Shanghai, China) for 30 min in the dark, washed, and imaged immediately. The parameters used for quantification were identical across the experimental groups.

NADH/NAD⁺ ratio detection

The NAD⁺ and NADH contents in the cells were detected using the WST-8 method via a NADH/NAD⁺ detection kit (S0175; Beyotime) and the NADH/NAD⁺ ratio was subsequently calculated. The detection steps were carried out according to the kit instructions and are briefly described as follows. For the prepared cell samples, after being washed with PBS, cell lysis buffer was added to lyse the cells. Next, a heat-treated sample for NADH determination and a sample directly used for the determination of the total amount of NAD⁺ and NADH were prepared. Then, ethanol dehydrogenase working solution was added to both samples, which were subsequently incubated in the dark. Finally, after the chromogenic solution was added and incubated, the OD value was measured on a microplate reader (Synergy H1; BioTek, Vermont, USA) at 450 nm, and the total amount of NAD⁺ and NADH and the content of NADH were calculated according to the standard curve. The content of NAD⁺ was obtained by subtracting the separately measured amount of NADH from the total amount of NAD⁺ and NADH.

Mitochondrial membrane potential assay

Tetramethylrhodamine ethyl ester (TMRE) staining was performed as previously described [22]. In brief, the cells were incubated with TMRE working solution (C2001S; Beyotime) for 15–45 min in the dark, washed with HBSS, and then counterstained with Hoechst 33342 for 5 min, followed by taking photos under the EVOS M7000 fluorescence microscope. Fluorescence images were captured within 30 min post-staining.

Dual-luciferase reporter assay

The *SIRT1* promoter (–2000 to +66 bp) was cloned and inserted into pGL3-Basic (Promega, Madison, USA). Mutant constructs with disrupted MEF2A binding sites (predicted by LASAGNA-Search 2.0 [28]) were generated via overlap PCR. 293T cells were cotransfected with a Renilla luciferase vector (phRL-TK; Promega) via Lipofectamine 3000 (Invitrogen). Luminescence was measured 48 h post-transfection via the Dual-Luciferase Reporter Gene Assay Kit (E1910; Promega) with a GloMax® Explorer luminometer (Promega).

Chromatin immunoprecipitation (ChIP)

ChIP analysis was performed via the SimpleChIP® Enzymatic Chromatin IP Kit (#9003; CST, Danvers, USA). Briefly, HUVECs were crosslinked with 1% formaldehyde for 10 min at room temperature, followed by quenching with 0.125 M glycine for 5 min at room temperature. The cells were harvested, washed twice with ice-cold PBS, and lysed in 1× ChIP lysis buffer supplemented with 1 mM DTT and 1× protease inhibitor cocktail (PIC; CST). Chromatin was digested with micrococcal nuclease (MNase; CST) at 37°C for 20 min to generate 150–300 bp fragments.

The digested chromatin was immunoprecipitated overnight at 4°C with 2 μg of ChIP-grade anti-MEF2A antibody (#9736; CST) or IgG control (#2729; CST) coupled to Protein A/G magnetic beads. After sequential washing with low-salt and high-salt buffers, the bound complexes were eluted with ChIP elution buffer. Crosslinks were reversed by incubation with 200 mM NaCl at 65°C for 4 h, followed by proteinase K treatment for 45 min at 45°C. DNA was purified via silica-membrane columns and quantified via qPCR with SYBR Green Master Mix (Roche, Rotkreuz, Switzerland). The primer sequences spanning the predicted MEF2A binding sites are listed in Supplementary Table S1.

Experimental animals

Male C57BL/6J mice (6 weeks old; Guangdong Experimental Animal Center, Foshan, China) were housed under specific pathogen-free conditions (23 ± 2°C, 60% humidity, 12-h light cycle). After AAV1 (1×10^{12} vg/mouse; vg, viral genome) delivery via the tail vein, the mice were fed with a high-fat diet (HF60; Research Diets, Foshan, China) for 16 weeks. All procedures followed Animal Research: Reporting of *In Vivo* Experiments (ARRIVE) guidelines and were approved by the Institutional Animal Care and Use Committee of Guangzhou Medical University (No. 2021-LCYJ-ZF-06).

Vascular-specific *Mef2a* knockdown

The endothelial-specific pAV[Icam2]-shMef2a-GFP AAV1 vector was engineered by packaging *Icam2* promoter-driven Mef2a shRNA into AAV serotype 1 particles. The *Mef2a*-knockdown group (shMef2a, $n = 20$) received pAV[Icam2]-shMef2a-GFP AAV1 injection, and the control groups (shNC, $n = 20$) received pAV[Icam2]-miR30-shRNA-GFP AAV1 containing scrambled sequences. The mice were administered with 5×10^{11} vg/mouse particles via tail vein injection. Following viral transduction, the animals were fed with a high-fat diet (HF60; Research Diets) containing 60% fat for 16 weeks to induce atherosclerosis.

Tissue harvesting

The mice were anesthetized via inhalation of 2% isoflurane, with the depth of anesthesia confirmed by the absence of the toe pinch reflex. Following euthanasia through cervical dislocation, terminal blood collection was performed via orbital enucleation via heparinized capillaries. Major organs, including the aortic arch, carotid bifurcation, hepatic lobe, and cardiac ventricles, were

immediately dissected. All the tissues were snap-frozen in liquid nitrogen or fixed in 4% paraformaldehyde (PFA; G1101; Servicebio, Wuhan, China) for subsequent analyses.

Vascular ROS detection

Fresh carotid artery cryosections (10 μm) were stained with 5 μM dihydroethidium (DHE; S0063; Beyotime) in PBS at 37°C for 30 min. After counterstaining with DAPI (1 μg/mL, 5 min) and PBS washes, the sections were mounted with ProLong® Gold Antifade Reagent (P36930; Thermo Fisher Scientific). Fluorescence imaging was performed via an LSM 880 confocal microscope (20× objective; Zeiss, Oberkochen, Germany) with identical exposure settings across groups.

Immunofluorescence staining

Paraformaldehyde-fixed vessels were embedded in paraffin and sectioned at a thickness of 5 μm. Antigen retrieval was conducted in EDTA buffer (pH 8.0, 95°C, 20 min), followed by endogenous peroxidase blockade with 3% H_2O_2. The sections were blocked with 5% BSA for 1 h before they were incubated with an anti-8-OHdG antibody (1:200, sc-393871; Santa Cruz Biotechnology, Dallas, USA) overnight at 4°C. Tyramide-FITC signal amplification (1:100) was performed after secondary antibody incubation. The nuclei were stained with DAPI (1 μg/mL, 5 min) prior to imaging on a Zeiss LSM 880 system (Zeiss).

RT-qPCR

Total RNA was isolated via TRIzol® (Invitrogen) with the following modifications for vascular tissues: Aortic segments were snap-frozen in liquid nitrogen and homogenized in a cryomill. The lysates were phase separated by the addition of chloroform (1:5, v/v) and centrifuged at 12,000 *g* (4°C, 15 min). The RNA was precipitated with ice-cold isopropanol (1:1, v/v), followed by washes with 75% ethanol. The RNA integrity was verified via 1% agarose gel electrophoresis. Reverse transcription was performed with FastKing RT SuperMix (KR123; Tiangen, Beijing, China) with genomic DNA removal. SYBR Green-based qPCR was performed on a LightCycler® 480 system (Roche). Relative expression levels of target genes were calculated with the $2^{-\Delta Ct}$ method. *Gapdh* was used as the internal control. The primer sequences for the human/mouse targets are listed in Supplementary Table S1.

Western blot analysis

Cells were extracted via RIPA buffer (50 mM Tris-HCl, pH 7.4, 1% NP-40, 0.5% sodium deoxycholate) supplemented with protease/phosphatase inhibitors (PICs; FD1002; Hangzhou Fdbio Technology, Hangzhou, China). For tissue homogenization, a tissue grinder at 60 Hz was used for 5 cycles (60 s/cycle). Lysates were cleared by centrifugation (12,000 *g*, 20 min, 4°C).

The protein concentration was determined via a BCA assay kit (23227; Thermo Fisher Scientific). The samples (30 μg/lane) were resolved on 10% SDS-PAGE gels and transferred to PVDF membranes (IPFL00010; Millipore, Burlington, USA). The membranes were blocked with 5% nonfat milk and probed with the following primary antibodies: anti-MEF2A, anti-SIRT1 (#9475; CST), anti-PGC-1α (#2178; CST), and loading controls: β-actin (#4970; CST) and GAPDH (#5174; CST). After incubation with primary antibodies, the membranes were incubated with horseradish peroxidase (HRP)-conjugated anti-rabbit IgG (7074; CST) diluted 1:5000 in 5% non-fat milk for 1 hour at room temperature. Protein bands were visualized using an enhanced chemiluminescence (ECL) substrate (FD8030; Fdbio Technology, Hangzhou, China) and imaged with a CCD-based imager (Unitec Cambridge Alliance Q9 System, Cambridge, UK). For band quantification, ImageJ was used with background subtraction.

Statistical analysis

The *in vitro* experiments were independently repeated over 3 times, and the data are expressed as the mean ± SEM. The mouse studies included ≥ 5 animals per group (biological replicates $n \geq 5$). Normality was assessed via the Shapiro-Wilk test. Parametric data were analyzed by two-tailed Student's *t* test; nonparametric data were analyzed via the Mann-Whitney U test. All analyses were performed in GraphPad Prism 8.0.1, with the significance threshold set at $P < 0.05$.

Results

MEF2A deficiency exacerbates oxidative stress via mitochondrial dysregulation

On the basis of our previous findings that MEF2A overexpression mitigates H_2O_2-induced endothelial senescence [27], we first investigated its role in redox homeostasis. HUVECs exposed to 200 μM H_2O_2 for 2 h presented an average 37.4% reduction in viability measured by CCK-8 assay (Figure 1A), paralleled by a marked downregulation of the MEF2A protein (an average 70% decrease; Figure 1B,C). Strikingly, *MEF2A* silencing recapitulated the oxidative phenotype of H_2O_2-treated cells: cellular ROS was increased by an average of 4.69-fold (Figure 1D), whereas mitochondrial ROS was increased by an average of 67% (Figure 1E). Redox imbalance was further evidenced by a 46.6% reduction in the GSH/GSSG ratio (Figure 1F), a 34% increase in the NADH/NAD^+ ratio (Figure 1G), and a 63.7% reduction in the mitochondrial membrane potential (Figure 1H). With the silencing of *MEF2A*, there was a sharp decrease in the mitochondrial membrane potential and a significant increase in the mitochondrial ROS level and the NADH/NAD^+ ratio, indicating that the strong oxidative stress caused by MEF2A deficiency is due mainly to the collapse of mitochondrial function.

MEF2A orchestrates the SIRT1/PGC-1α axis to sustain redox homeostasis

Given the established role of SIRT1/PGC-1α in regulating mitochondrial integrity [29], we hypothesized that this pathway may mediate the antioxidant effects of MEF2A. Silencing *MEF2A* reduced SIRT1 and PGC-1α protein levels by an average of 34.4% and 38.8%, respectively (Figure 2A–D). Notably, *SIRT1* knockdown recapitulated MEF2A deficiency, increasing the levels of cellular ROS (2.4-fold; Figure 2E) and mitochondrial ROS (Supplementary Figure S1), disrupting the NADH/NAD^+ balance (31.8% increase in the NADH/NAD^+ ratio; Figure 2F), reducing the GSH/GSSG ratio by 46% (Figure 2G), and reducing the mitochondrial membrane potential by 53.6% (Figure 2H). Rescue experiments were performed to confirm functional interdependence. SIRT1 overexpression ameliorated *MEF2A* knockdown-induced PGC-1α suppression (Figure 2A–D) and restored all cellular phenotypes, including suppressing cellular ROS (Figure 2E) and mitochondrial ROS (Supplementary Figure S1), normalizing the NADH/NAD^+ ratio (Figure 2F), increasing the GSH/GSSG ratio (Figure 2G), and rescuing the mitochondrial membrane

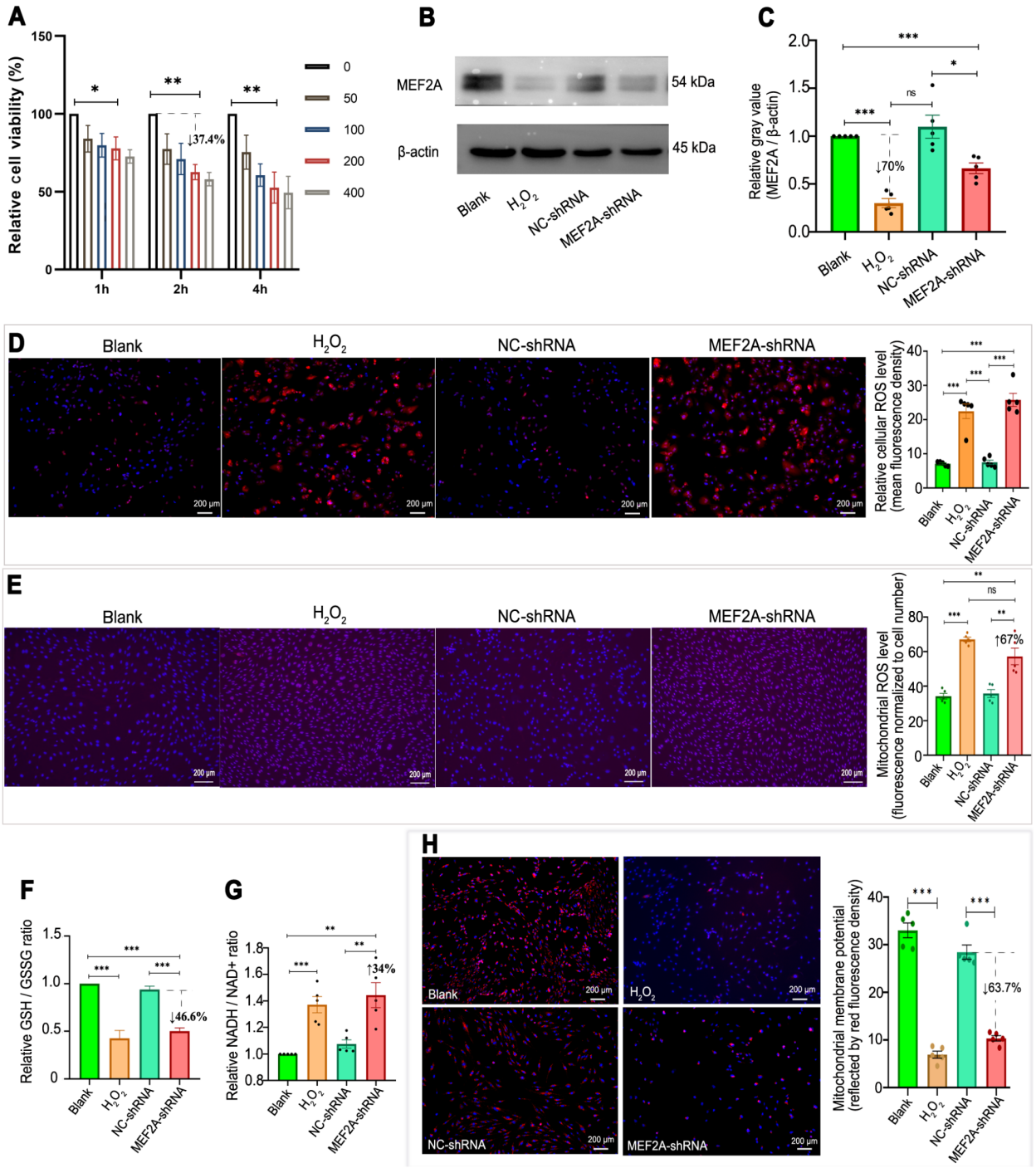


Figure 1. Modulation of MEF2A expression affects oxidative stress parameters in a cell model (A) The bar graphs illustrate the viability of HUVECs upon exposure to different concentrations (μM) of H_2O_2 for different durations (hours) in comparison with the control group. (B) Western blots showing the bands corresponding to MEF2A (54 kDa) and β-actin (45 kDa) as loading controls. (C) The bar plot depicts the grayscale quantification of the MEF2A protein levels relative to those in the blank group after normalization to β-actin. (D) Fluorescence microscopy images of HUVECs stained with dihydroethidium were obtained to evaluate the levels of reactive oxygen species (ROS). Increased red fluorescence indicates increased ROS levels. The bar graphs show the mean relative fluorescence intensity normalized to the number of cells in each group. (E) Fluorescence microscopy images of HUVECs stained with an OM08 (BestBio, equivalent to MitoSOX™ Red from Thermo) probe were obtained to evaluate the levels of mitochondrial ROS (mt-ROS). Increased red fluorescence indicates increased mt-ROS levels. The bar graphs display the mt-ROS normalized to the number of cells in the different groups. (F) Bar graphs showing the GSH/GSSG ratio relative to that of the control group. (G) Bar graphs showing the NADH/NAD^+ ratio relative to that of the control group. (H) Fluorescence microscopy images of HUVECs stained with tetramethylrhodamine ethyl ester (TMRE) were used to assess the mitochondrial membrane potential. The bar graph shows the fluorescence intensity normalized to the number of cells. DAPI was used to stain the cell nucleus blue. The data for all the bar plots are presented as the mean ± standard error from multiple independent experiments (n = 3–5). Student's t test was used to compare the significance of differences between two groups. *P < 0.05, **P < 0.01, and ***P < 0.001.

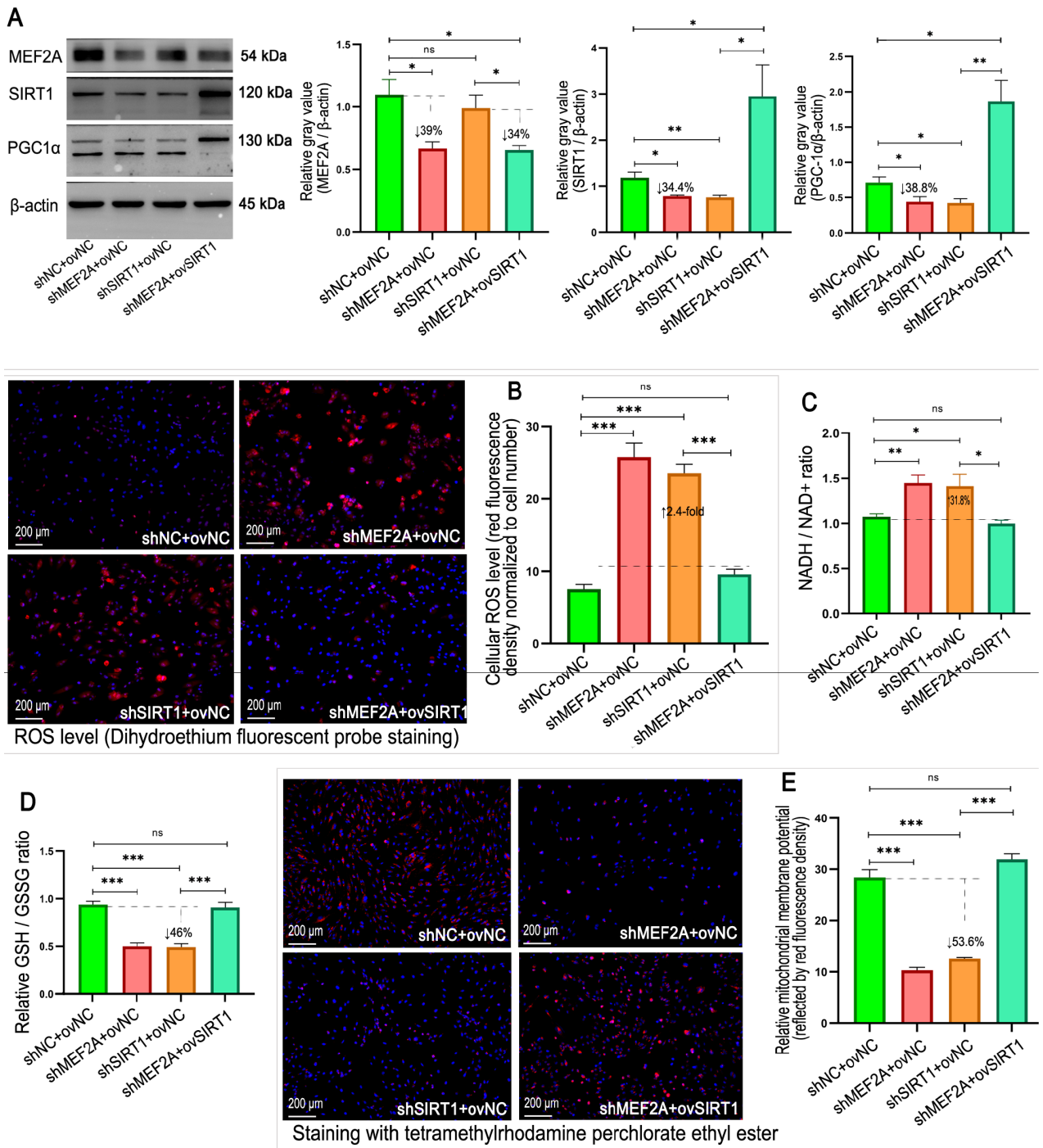


Figure 2. Influence of *MEF2A* silencing on SIRT1/PGC-1α expression and cellular oxidative stress (A) Western blot bands of various proteins (β-actin band as the loading control). (B–D) The bars represent the relative expression levels of MEF2A (B), SIRT1 (C), and PGC-1α (D), with the grayscale values normalized to those of β-actin. (E) Fluorescence microscopy images of HUVECs subjected to different interventions involving MEF2A or SIRT1 were obtained. The increase in red fluorescence indicates an increase in the level of ROS. Corresponding bar graphs were used to depict the relative average ROS levels in each group, providing a quantitative comparison. (F) Bar graphs showing the mean relative NADH/NAD$^+$ ratio for each group. (G) The mean relative GSH/GSSG ratio per group is presented in the bar graphs. (H) Fluorescence microscopy images of HUVECs stained with TMRE for the detection of the mitochondrial membrane potential are shown. Accompanying bar charts of the mean relative fluorescence intensity per group are also provided to facilitate comparisons among different groups. DAPI was used to stain the cell nucleus blue. The data for all the bar plots are presented as the mean ± standard error from multiple independent experiments (n = 3–5). Student's t test was used to compare the significance of differences between two groups. shMEF2A represents *MEF2A* silencing, shSIRT1 represents *SIRT1* silencing, shNC represents the negative control shRNA, and ov-NC represents the negative control overexpression plasmid. *$P < 0.05$, **$P < 0.01$, and ***$P < 0.001$. ns, not significant.

potential (Figure 2H). These data establish MEF2A as a critical upstream regulator that functionally sustains the SIRT1/PGC-1α axis, which is essential for redox and mitochondrial homeostasis.

MEF2A overexpresion may be a highly effective new method for antioxidant therapy through the SIRT1/PGC-1α axis

Following the overexpression of MEF2A in HUVECs, SIRT1 (Figure 3A,C) and PGC-1α (Figure 3A,D) expressions were significantly upregulated. Overexpressing SIRT1 did not affect the expression of MEF2A (Figure 3A,B). When *SIRT1* was silenced simultaneously with the overexpression of MEF2A, the expression level of SIRT1 did not significantly change compared with that in the negative control group (Figure 3A,C). Overexpressing MEF2A produced the same antioxidative stress effects as overexpressing SIRT1, including a significant reduction in the cellular ROS level (Figure 3E), mitochondrial ROS level (Figure 3F), and NADH/NAD^+ ratio (Figure 3G) in H_2O_2-treated cells, a significant increase in the GSH/GSSG ratio (Figure 3H), and a significant increase in the mitochondrial membrane potential (Figure 3I). When cells were treated with H_2O_2 while *SIRT1* was silenced simultaneously with the overexpression of MEF2A, the cellular effects were consistent with those of the negative control group (Figure 3E–I). These results indicate that MEF2A and SIRT1 overexpressions have almost identical antioxidant effects and that MEF2A overexpression achieves its antioxidant function by upregulating the expression of SIRT1.

MEF2A directly transactivates SIRT1 via conserved promoter elements

Although previous studies have suggested that MEF2A regulates the expression of SIRT1, the molecular mechanism by which MEF2A regulates SIRT1 expression is not fully understood. Here, mechanistic dissection revealed two evolutionarily conserved MEF2A binding motifs in the *SIRT1* promoter: motif-1 (−392/−377 bp) and motif-2 (−904/−889 bp) (Figure 4A). Luciferase assay results revealed that the activity of the wild-type *SIRT1* promoter exceeded that of the mutant control by 43% under basal conditions (Figure 4B) and by 77% upon MEF2A overexpression (Figure 4C). Furthermore, compared with basal conditions, coexpressing MEF2A increased wild-type *SIRT1* promoter activity by 73% (Figure 4D). ChIP was performed to validate the direct binding. It was found that anti-MEF2A enriched *SIRT1* promoter fragments by >10-fold compared with the anti-IgG controls (Figure 4E–G). This transcriptional regulation is unidirectional, as *SIRT1* knockdown did not alter MEF2A level (Figure 2A), suggesting that MEF2A is a primary driver of SIRT1 expression.

Collectively, these *in vitro* experimental results suggest that unlocking the MEF2A-SIRT1 master switch may be a novel paradigm for targeted antioxidant therapy.

Endothelial-specific *Mef2a* knockdown recapitulates vascular oxidative pathology *in vivo*

To validate the antioxidant role of MEF2A in vascular tissues *in vivo*, we generated endothelial-specific *Mef2a*-knockdown C57BL/6J mice and fed them with a high-fat diet (HFD) for four months to assess vascular pathology and gene expression alterations.

Fluorescence imaging of fresh carotid artery sections revealed robust GFP expression throughout the vascular wall (Figure 5A), confirming successful AAV1 transduction and transgene expression in vascular tissues. Faint green fluorescence was also observed in frozen sections of liver, kidney, spleen, and lung tissues (data not shown). While this signal may originate from the abundant microvasculature within these organs, the endothelial specificity of MEF2A expression was confirmed through tissue-specific knockdown efficacy analysis. Western blot analysis revealed unchanged MEF2A levels in liver (Figure 5B) and heart tissues (Figure 5C) but significantly decreased MEF2A levels in aortic tissues compared with those in controls (Figure 5D,E). Compared with control mice, *Mef2a*-knockdown mice fed with an HFD for 16 weeks presented increased body weight gain (Figure 5F), whereas plasma lipid profiles (total cholesterol, HDL-C, LDL-C) and blood glucose levels remained unchanged (Figure 5G–J). Notably, the level of circulating triglycerides was markedly elevated in the knockdown group (Figure 5K).

Oil Red O staining revealed significantly increased lipid deposition in aortic arches (Figure 6A). The plasma GSH/GSSG ratio was substantially reduced (Figure 6B), and tissue ROS level was significantly increased (Figure 6C). Vascular 8-hydroxy-2′-deoxyguanosine (8-OHDG) level, a biomarker of ROS-mediated DNA damage [30], was elevated (Figure 6D). These data indicate that *Mef2a* silencing increases atherogenesis, systemic redox imbalance, and DNA oxidative damage.

Western blot and RT-qPCR analyses confirmed the coordinated downregulation of both *Sirt1* and *Pgc1a* in aortic tissues from *Mef2a*-knockdown mice, with significant reductions observed at both protein (Figure 7A–F) and mRNA levels (Figure 7G–I). The results shown in Figures 5D and 7A were derived from different individuals within the corresponding groups of the same cohort of *Mef2a*-knockdown mice and their negative control mice. This *in vivo* validation aligns with our *in vitro* findings, demonstrating that MEF2A deficiency promotes vascular oxidative stress and DNA damage through the suppression of the SIRT1/PGC-1α axis.

Discussion

Our study establishes MEF2A as a central transcriptional orchestrator of vascular redox homeostasis that functions through direct governance of the SIRT1/PGC-1α axis. While oxidative stress is universally acknowledged as a pivotal mechanism underlying endothelial dysfunction and atherosclerotic progression [31–33], contemporary therapeutic strategies remain ineffective in targeting its fundamental molecular drivers [34]. The present work demonstrated that MEF2A deficiency led to a catastrophic redox imbalance characterized by uncontrolled reactive oxygen species (ROS) generation, glutathione system collapse, and mitochondrial dysfunction—pathological hallmarks mirroring advanced atherosclerosis [35]. Crucially, MEF2A overexpression not only reversed these abnormalities but also restored physiological redox signaling, establishing its indispensable role in vascular antioxidant defense.

The mechanistic hierarchy of MEF2A-mediated protection operates through coordinated regulation of mitochondrial quality control systems. Chromatin occupancy studies confirmed that MEF2A binds to evolutionarily conserved cis-regulatory elements within the *SIRT1* promoter, driving the transcriptional activation essential for maintaining SIRT1 expression. This genomic control synergizes with posttranslational modulation of nicotinamide adenine dinucleotide (NAD^+) metabolism, wherein MEF2A signaling stabilizes the cellular NAD^+ pools required for SIRT1 deacetylase activity [36–38]. In addition to these mechanisms, MEF2A induces

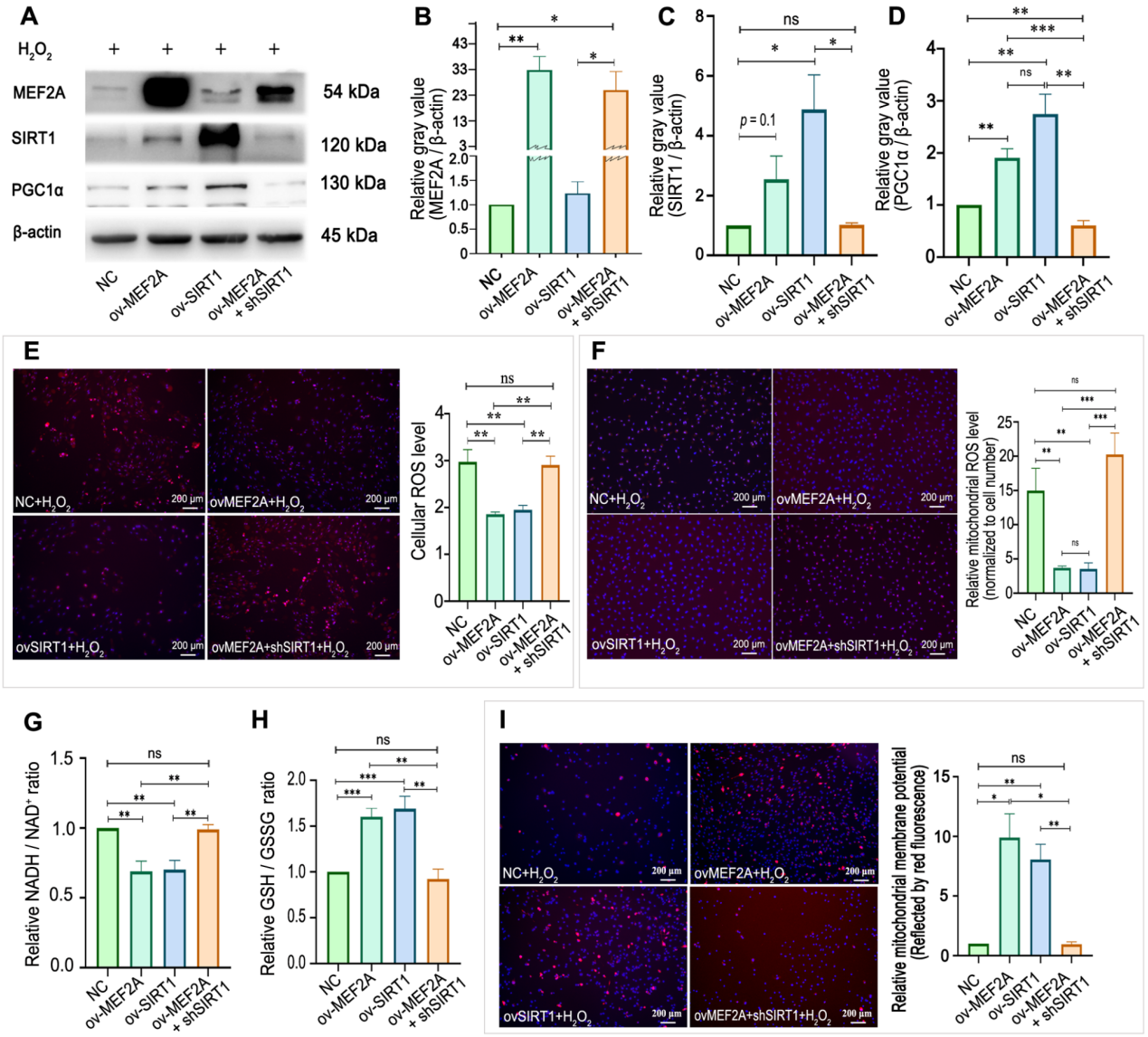


Figure 3. Effects of MEF2A overexpression on oxidative stress and the SIRT1/PGC-1α pathway (A) Western blot bands of various proteins (β-actin band as the loading control). (B–D) The bars represent the relative expression levels of MEF2A (B), SIRT1 (C), and PGC-1α (D), with the grayscale values normalized to those of β-actin. (E) Fluorescence microscopy images of HUVECs stained with dihydroethidium were obtained to evaluate the levels of the cellular ROS. Increased red fluorescence indicates increased ROS levels, with bar graphs representing relative average ROS levels per group. (F) Fluorescence microscopy images of HUVECs stained with the OM08 probe were obtained to evaluate the levels of mitochondrial ROS (mt-ROS). Increased red fluorescence indicates increased mt-ROS levels. The bar graphs display the mt-ROS normalized to the number of cells in the different groups. (G) Bar graphs illustrating the mean relative NADH/NAD$^+$ ratio for each group. (H) Bar graphs depicting the mean relative GSH/GSSG ratio per group. (I) Fluorescence microscopy images of HUVECs stained with TMRE to assess the mitochondrial membrane potential, with bar charts showing the mean relative fluorescence intensity per group. DAPI was used to stain the cell nucleus blue. The data for all the bar plots are presented as the mean±standard error from multiple independent experiments (n = 3–5). Student's t test was used to compare the significance of differences between two groups. ov-MEF2A, MEF2A overexpression; ov-SIRT1, SIRT1 overexpression; NC, negative control. *P < 0.05, **P < 0.01, and ***P < 0.001. ns, not significant.

PGC-1α expression to optimize mitochondrial biogenesis while suppressing electron transport chain-derived ROS leakage [12,13,39,40]. Collectively, these findings elucidate the critical role of MEF2A in maintaining vascular redox homeostasis through direct transcriptional activation of SIRT1, thereby modulating the SIRT1/PGC-1α axis. This finding not only advances our understanding of vascular oxidative stress regulation but also identifies a potential therapeutic target for oxidative cardiovascular diseases.

Oxidative stress, characterized by an imbalance between ROS production and antioxidant defenses, is a key contributor to cardiovascular pathologies such as atherosclerosis and hypertension. In atherosclerosis, redox imbalance promotes lipid peroxidation, particularly of low-density lipoprotein (LDL), leading to the formation of oxidized LDL (oxLDL) and subsequent endothelial dysfunction, inflammation, and foam cell formation—hallmarks of plaque development [41,42]. Similarly, in hypertension, metabolic disruptions such as glucose-6-phosphate dehydrogenase (G6PD) deficiency induce a metabolic switch that exacerbates oxidative

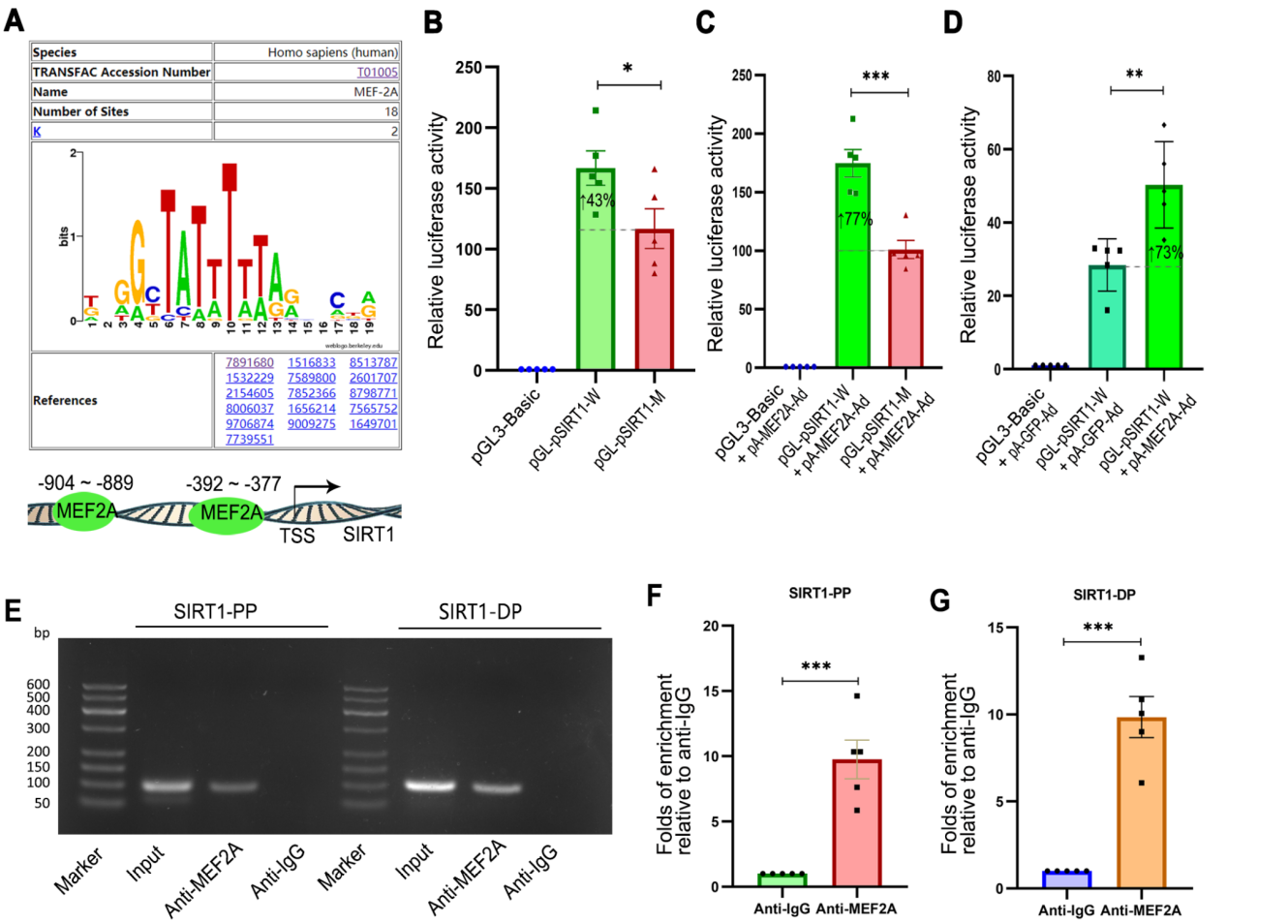


Figure 4. Prediction and validation of MEF2A binding sites in the *SIRT1* promoter region (A) Characteristic sequence of MEF2A binding sites and a schematic of MEF2A binding in the *SIRT1* promoter region, as predicted by TF-Search2.0. (B) The relative luciferase activity was calculated by dividing the normalized value of each group in each experiment (firefly luciferase activity/Renilla luciferase activity) by the normalized value of the control group (pGL3-basic). (C) The relative luciferase activity was calculated by dividing the normalized value of each group in each experiment (firefly luciferase activity/Renilla luciferase activity) by the normalized value of the control group (pGL3-basic + pA-MEF2A-Ad). (D) The relative luciferase activity was calculated by dividing the normalized value of each group in each experiment (firefly luciferase activity/Renilla luciferase activity) by the normalized value of the control group (pGL3-basic + pA-GFP-Ad). (E) Gel electrophoresis results of PCR products amplified from DNA fragments pulled down by different antibodies in ChIP. (F,G) Quantitative analysis of SIRT1 proximal and distal promoter DNA fragments pulled down by anti-MEF2A via qPCR. The enrichment fold change was calculated via the formula $2^{-\Delta Ct}$ ($\Delta Ct = Ct_{anti\text{-}MEF2A} - Ct_{anti\text{-}IgG}$). The data for all the bar plots are presented as the mean ± SEM. All experiments were performed in at least three independent replicates. Student's *t* test was used to compare the significance of differences between two groups. $^{*}P < 0.05$, $^{**}P < 0.01$, and $^{***}P < 0.001$. pGL3-basic, luciferase plasmid without a promoter; pGL-pSIRT1-W, luciferase plasmid with the wild-type *SIRT1* promoter; pGL-pSIRT1-M, luciferase plasmid with the *SIRT1* promoter mutated at the predicted MEF2A binding sites. pA-MEF2A-Ad, adenovirus expressing MEF2A. SIRT1-PP, DNA fragment near MEF2A binding sites in the proximal *SIRT1* promoter; SIRT1-DP, DNA fragment near MEF2A binding sites in the distal *SIRT1* promoter.

stress, driving pulmonary vascular remodeling and hypertension [43]. These mechanisms underscore the therapeutic potential of targeting redox imbalance in cardiovascular diseases.

The SIRT1/PGC-1α pathway is central to mitochondrial quality control and antioxidant defense, making it a focal point in cardiovascular research. SIRT1, an NAD^+-dependent deacetylase, deacetylates and activates PGC-1α, a master regulator of mitochondrial biogenesis and ROS detoxification [29,44]. This axis is critical for preserving endothelial function and mitigating oxidative damage [12,37]. Recent studies highlighted its therapeutic relevance: compounds such as urolithin A and resveratrol activate SIRT1/PGC-1α to ameliorate mitochondrial dysfunction and oxidative stress in models of Parkinson's disease and diabetic nephropathy [14,22,45]. Deeper mechanistic exploration of this pathway, including its upstream regulators (*e.g.*, MEF2A) and downstream effectors (*e.g.*, mitochondrial dynamics), could unveil novel strategies to counteract oxidative cardiovascular diseases.

These mechanistic insights carry profound therapeutic implications that challenge conventional antioxidant paradigms. Current clinical failures in redox-targeted interventions stem from two fundamental limitations: nonspecific ROS scavenging, which disrupts physiological signaling, and inadequate attention to the transcriptional networks governing endogenous defense systems [42,46,47]. Our results suggest that MEF2A activation is a precision therapeutic strategy that simultaneously enhances mitochondrial integrity upon the upregulation of SIRT1/PGC-1α, bolsters endo-

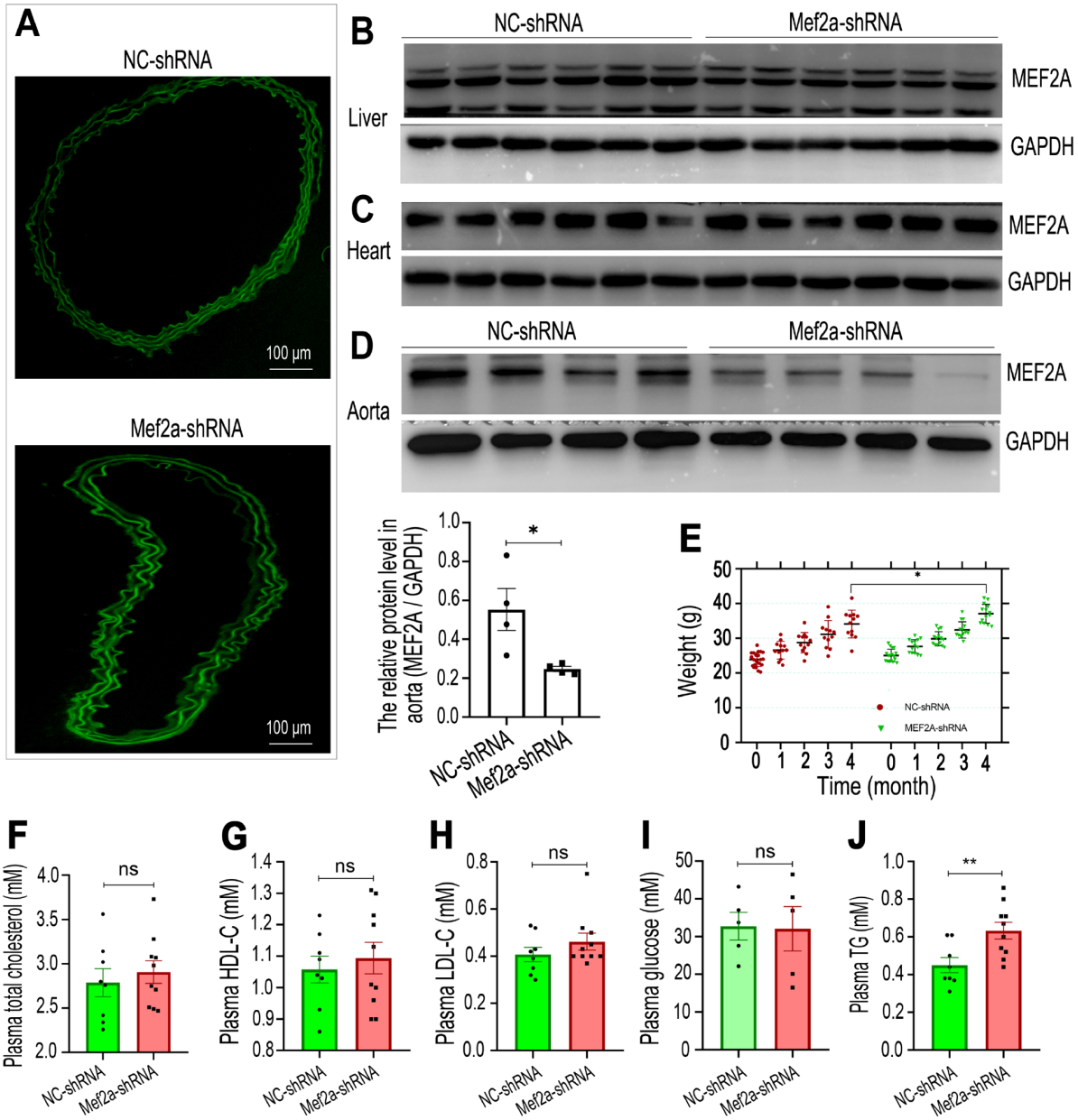


Figure 5. Targeted knockdown of *Mef2a* in mouse blood vessels and its physiological effects (A) Fluorescence microscopy images of carotid frozen sections showing the expression of GFP in the vascular ring. The upper image represents the NC-shRNA group, and the lower image represents the Mef2a-shRNA (*Mef2a* knockdown) group, with a scale bar of 100 μm. (B–D) Western blot analysis were used to assess the expression levels of MEF2A in different tissues. (B) MEF2A expression in the mouse liver ($n = 6$ biological replicates). (C) MEF2A expression in the mouse heart ($n = 6$ biological replicates). (D) MEF2A expression in the mouse aorta ($n = 4$ biological replicates). (E) The bar chart with a scatter plot indicates the relative protein level of MEF2A in the aorta quantified by grayscale value analysis. There are only 4 biological replicates of aortic tissue here, which is less than those of liver and heart tissue, mainly because aortic tissue needs to be used for more detection, such as Oil Red O staining and mRNA extraction. These 4 aortic tissues were obtained from an independent set of biological replicates compared to the 5 aortic tissues used in Figure 7. (F) Comparison of mouse weights between the NC and *MEF2A*-shRNA groups at various time points during a high-fat diet. The data are represented by a scatter plot with medians and interquartile ranges. (G–K) The bar charts with scatter plots indicate the relative levels of blood lipids and glucose after 4 months of feeding between the NC and *MEF2A*-shRNA groups. The data are presented as the mean ± SEM. (G) Total plasma cholesterol levels. (H) Plasma high-density lipoprotein cholesterol (HDL-C) levels. (I) Plasma low-density lipoprotein cholesterol (LDL-C) levels. (J) Plasma glucose levels. (K) Plasma triglyceride (TG) levels. GAPDH was used as a loading control for the western blot analysis. The data for all the bar plots are presented as the mean ± SEM. Student's *t* test or Mann Whiteley U test was used to compare the significance of differences between two groups. $^*P < 0.05$ and $^{**}P < 0.01$. ns, not significant.

genous antioxidant capacity, and preserves redox-sensitive vascular homeostasis. The spatial specificity of this regulation is particularly noteworthy—endothelial-restricted *MEF2A* knockdown in murine models induced severe vascular oxidative pathology while sparing cardiac and hepatic tissues, suggesting that cell type-specific delivery systems could maximize therapeutic efficacy while

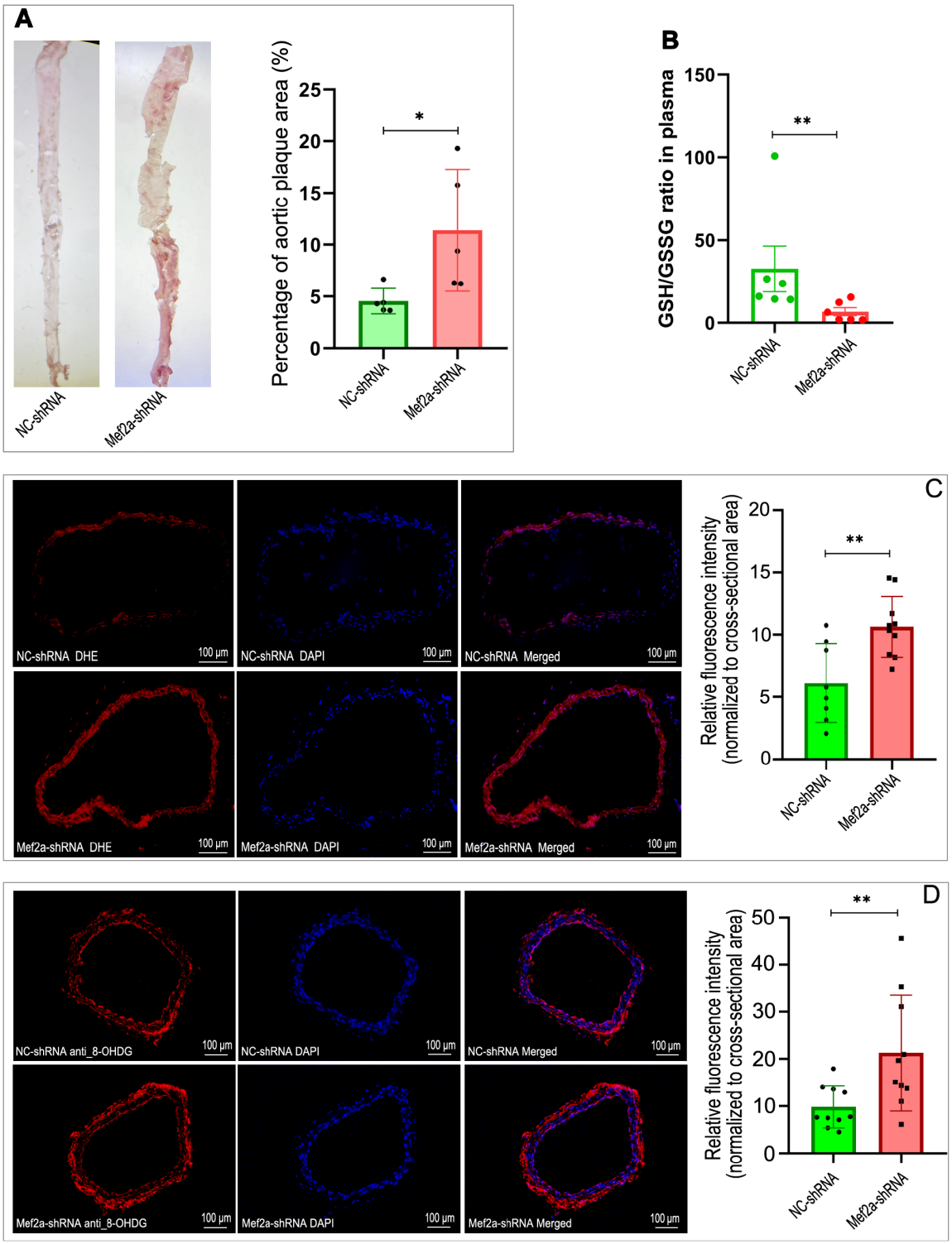


Figure 6. Pathological alterations in mice with specific *Mef2a* knockdown in blood vessels (A) Enface staining of the aorta with Oil Red O. The combined bar scatter plot shows the mean percentage of the aortic plaque area. (B) The combined bar scatter plot shows the mean values of the plasma GSH/GSSG ratio for each group. (C) Fluorescence microscopy images of frozen carotid sections were obtained after staining with a dihydroethidium (DHE) probe to evaluate the levels of ROS. Red fluorescence indicates a high level of ROS. The combined bar scatter plot shows the mean relative red fluorescence intensity normalized to the vascular ring area for each experimental group. (D) Fluorescence microscopy images of paraffin-embedded carotid sections incubated with an antibody against 8-OHDG. Red fluorescence indicates the generation of 8-OHDG, which is a marker of DNA damage. The combined bar scatter plot shows the mean relative red fluorescence intensity normalized to the vascular ring area for each experimental group. DAPI was used to stain the cell nucleus blue. The data in the bar plots are presented as the mean ± SEM. Student's *t* test was used to compare the significance of differences between two groups. $^{*}P < 0.05$ and $^{**}P < 0.01$.

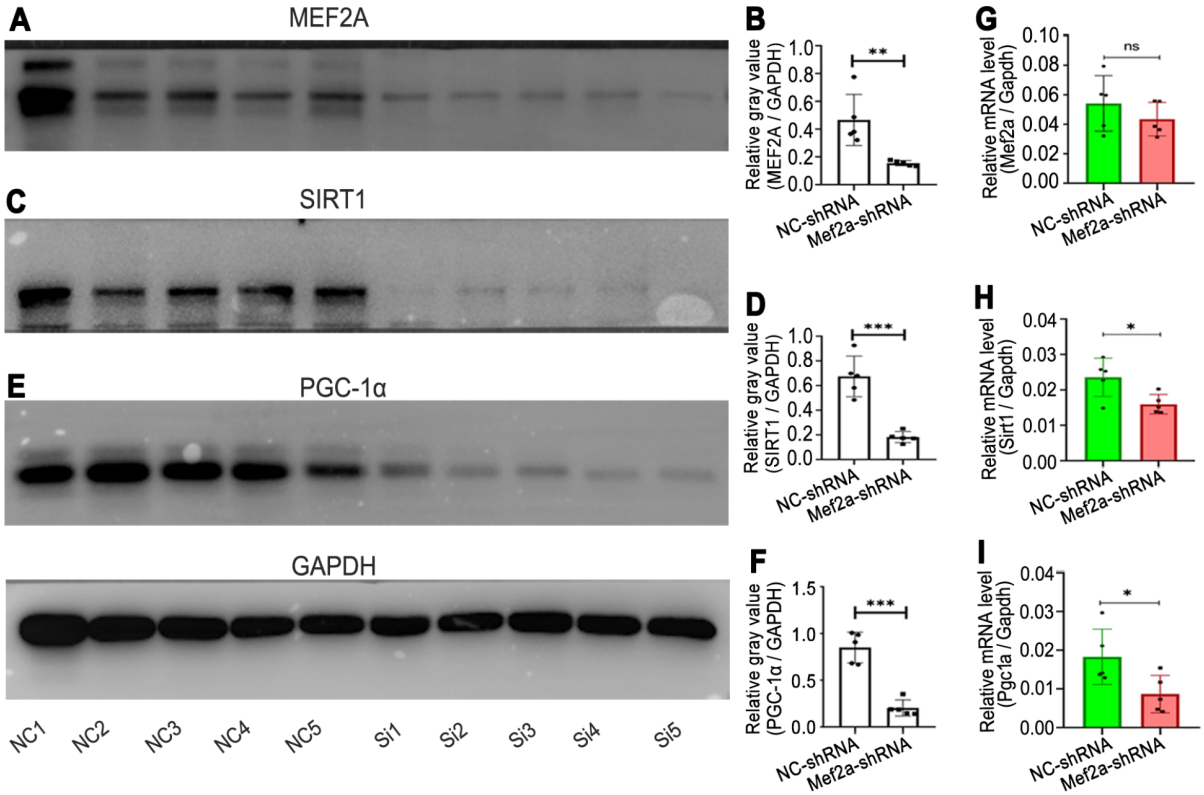


Figure 7. Western blot and quantitative real-time PCR (qPCR) analyses of gene expression in the mouse aorta (A,C,E) Western blot analyses were performed for the MEF2A (A), SIRT1 (C), and PGC-1α (E) proteins via the appropriate antibodies. Lanes NC1–NC5 and Si1–Si5 represent different negative control (NC) and *Mef2a*-knockdown (Si) samples from 5 biological replicates, with GAPDH serving as a loading control. (B,D,F) The relative protein levels of MEF2A (B), SIRT1 (D), and PGC-1α (F) were quantified via grayscale value analysis. The combined bar scatter plot presents the data as the mean ± SEM. (G,H,I) qRT-PCR was used to analyze the mRNA levels of *Mef2a* (G), *Sirt1* (H), and *Pgc1a* (I). The combined bar scatter plot shows the mRNA levels relative to that of the internal reference gene (*Gapdh*). The data for all the bar plots are presented as the mean ± SEM. Student's *t* test was used to compare the significance of differences between two groups. $^{*}P < 0.05$, $^{**}P < 0.01$, and $^{***}P < 0.001$ between the NC and *Mef2a* knockdown groups. ns, not significant.

minimizing off-target effects.

Elucidating the dual roles of MEF2A in vascular protection and disease pathogenesis requires understanding its compartment-specific biology. Although MEF2A is the core transcription factor for myocardial cell hypertrophy [48], our findings reveal a protective endothelial role through nuclear SIRT1/PGC-1α activation. This apparent paradox resolves through subcellular localization dynamics: nuclear MEF2A in the vascular endothelium promotes redox homeostasis, whereas cytoplasmic MEF2A in cardiomyocytes may drive pathological hypertrophy through calcineurin-dependent mechanisms [49]. Such tissue-specific functionality underscores the importance of developing targeted delivery platforms that exploit the protective capacity of MEF2A without activating deleterious pathways in other cell types.

The molecular mechanisms by which MEF2A regulates redox balance are likely multifaceted. Although our study revealed that MEF2A exerts antioxidative stress effects primarily by directly regulating SIRT1 to upregulate PGC-1α, some reports have suggested that MEF2A can directly modulate PGC-1α to promote mitochondrial biogenesis in gastric cancer cells [50]. It may even enhance mitochondrial ROS clearance by inhibiting KEAP1 to stabilize NRF2, thereby exerting antioxidative effects [50]. These findings indicate that MEF2A may employ multiple parallel pathways to perform its antioxidative functions. The predominant pathway may vary depending on the cell type and specific microenvironment under physiological or pathological conditions. Notably, our study revealed that MEF2A not only promotes SIRT1 expression but also may increase SIRT1 activity by increasing NAD^+ levels. Collectively, these studies demonstrate that MEF2A activates the antioxidant system through diverse mechanisms. In drug screening, adopting MEF2A upregulation as a criterion for selecting antioxidative agents might prove to be a more effective strategy. Indeed, the protective effect of the antioxidant resveratrol on vascular endothelial cells depends on the upregulation of MEF2A expression [22].

The evolutionary conservation of MEF2 family proteins offers additional insights into their therapeutic potential. In Drosophila and mammals, MEF2 homologs play dual roles in stress adaptation and metabolic regulation—an ancient functional duality that modern medicine might exploit [51,52]. Our finding that MEF2A coordinates mitochondrial renewal through SIRT1/PGC-1α parallels its role in maintaining muscle mitochondrial networks during aging, suggesting conserved mechanisms for combating oxidative decline across tissues.

Despite these advances, several critical questions must guide future investigations. First, the cell type-specific effects of MEF2A

modulation in complex vascular ecosystems remain incompletely characterized [15]. While our work established endothelial MEF2A as a master redox regulator, its potential roles in vascular smooth muscle cell phenotypic switching or macrophage polarization during atherogenesis warrant systematic exploration. Single-cell transcriptomic analyses of atherosclerotic plaques could delineate compartment-specific regulatory networks and identify cell populations most amenable to MEF2A-targeted interventions. Second, the integration of MEF2A signaling with biomechanical forces requires elucidation. Given the established mechanosensitivity of MEF2A and the well-documented atheroprotective effects of laminar shear stress [53,54], investigating the potential synergy between hemodynamic forces and MEF2A activation could inform both pharmacological strategies and device-based therapies. Third, the functional speculation of MEF2A in atherosclerosis relies heavily on murine models; however, it is crucial to note the substantial biological differences between human and murine vasculature. Notably, murine atherosclerosis models lack key human-specific pathological features, such as fibrous cap composition and plaque calcification dynamics [55]. These limitations necessitate translational validation in larger animal models or human vascular systems to confirm their clinical relevance. Fourth, while our ChIP assay provides evidence that MEF2A directly binds to the predicted cis-elements in the promoter of *SIRT1*, the assay regions limited to the predicted binding sites may overlook potential indirect interactions between MEF2A and the lateral cis-elements. To obtain compelling evidence for the direct binding of proteins to specific DNA regions, the method used by Xie *et al.*[56] deciphering the binding sites of H3K18la in the *LCN2* promoter is worthy of recommendation.

In conclusion, this study establishes MEF2A as a central regulator of vascular redox homeostasis through coordinated activation of the SIRT1/PGC-1α axis and NAD^+ stabilization.

Supplementary Data

Supplementary data are available at *Acta Biochimica et Biophysica Sinica* online.

Acknowledgement

We would like to express our gratitude to the graduate students Yang Ji, Yichao Deng, Huanzhen Chen, and Changnong Chen from the Second Affiliated Hospital of Guangzhou Medical University for their assistance in experimental methods and processes.

Funding

This work was supported by the grants from the Guangzhou Municipal Science and Technology Project (No. 2024A03J0940 to B.L.), the Graduate Research Project of the Guangzhou Education Bureau (No. 2024312106 to B.L.), the Key Medical Disciplines and Specialties Program of Guangzhou (No. 2025–2027 to S.M.L.), and the Innovation Team of General Universities in Guangdong Province (No. 2023KCXTD025 to S.M.L.).

Conflict of Interest

The authors declare that they have no conflict of interest.

References

1. Akiyama Y, Ivanov P. Oxidative stress, transfer RNA metabolism, and protein synthesis. *Antioxid Redox Signal* 2024, 40: 715–735
2. Huang X, Zhou Y, Guo Y, Yan D, Sun P, Cao Y, Chen Y, *et al.* Selenium-doped copper formate nanozymes with antisenescence and oxidative stress reduction for atherosclerosis treatment. *Nano Lett* 2025, 25: 2662–2669
3. Zheng Y, Shao M, Zheng Y, Sun W, Qin S, Sun Z, Zhu L, *et al.* PPARs in atherosclerosis: the spatial and temporal features from mechanism to druggable targets. *J Adv Res* 2025, 69: 225–244
4. Griendling KK, Camargo LL, Rios FJ, Alves-Lopes R, Montezano AC, Touyz RM. Oxidative stress and hypertension. *Circ Res* 2021, 128: 993–1020
5. Kibel A, Lukinac AM, Dambic V, Juric I, Selthofer-Relatic K, Daiber A. Oxidative stress in ischemic heart disease. *Oxid Med Cell Longev* 2020, 2020: 1–30
6. Shaito A, Aramouni K, Assaf R, Parenti A, Orekhov A, Yazbi AE, Pintus G, *et al.* Oxidative stress-induced endothelial dysfunction in cardiovascular diseases. *Front Biosci (Landmark Ed)* 2022, 27: 105
7. Lennicke C, Cochemé HM. Redox metabolism: ROS as specific molecular regulators of cell signaling and function. *Mol Cell* 2021, 81: 3691–3707
8. Xu S, Ilyas I, Little PJ, Li H, Kamato D, Zheng X, Luo S, *et al.* Endothelial dysfunction in atherosclerotic cardiovascular diseases and beyond: from mechanism to pharmacotherapies. *Pharmacol Rev* 2021, 73: 924–967
9. Chiu T-H, Ku C-W, Ho T-J, Tsai K-L, Yang Y-D, Ou H-C, Chen H-I. Schisanhenol amelioratesoxLDL-caused endothelial dysfunction by inhibitingLOX-1 signaling. *Environ Toxicol* 2023, 38: 1589–1596
10. Gimbrone MA, García-Cardeña G. Endothelial cell dysfunction and the pathobiology of atherosclerosis. *Circ Res* 2016, 118: 620–636
11. Malekmohammad K, Sewell RDE, Rafieian-Kopaei M. Antioxidants and atherosclerosis: mechanistic aspects. *Biomolecules* 2019, 9: 301
12. Sarmah D, Datta A, Rana N, Suthar P, Gupta V, Kaur H, Ghosh B, *et al.* SIRT-1/RHOT-1/PGC-1α loop modulates mitochondrial biogenesis and transfer to offer resilience following endovascular stem cell therapy in ischemic stroke. *Free Radical Biol Med* 2024, 225: 255–274
13. Olmos Y, Sánchez-Gómez FJ, Wild B, García-Quintans N, Cabezudo S, Lamas S, Monsalve M. SirT1 Regulation of Antioxidant Genes Is Dependent on the Formation of a FoxO3a/PGC-1α Complex. *Antioxid Redox Signal* 2013, 19: 1507–1521
14. Carrizzo A, Iside C, Nebbioso A, Carafa V, Damato A, Sciarretta S, Frati G, *et al.* SIRT1 pharmacological activation rescues vascular dysfunction and prevents thrombosis in MTHFR deficiency. *Cell Mol Life Sci* 2022, 79: 410
15. Liu B, Ou WC, Fang L, Tian CW, Xiong Y. Myocyte enhancer factor 2a plays a central role in the regulatory networks of cellular physiopathology. *Aging Dis* 2022: 0
16. Ahmad AA, Meng-Jiao L, Lin J, Guo-Qing L. Myocyte enhancer factor 2 exerts a pivotal role in larval development in *Henosepilachna vigintioctopunctata*. *J Asia-Pac Entomol* 2024, 27: 1–9
17. Zhong R, Miao R, Meng J, Wu R, Zhang Y, Zhu D. Acetoacetate promotes muscle cell proliferation via the miR-133b/SRF axis through the Mek-Erk-MEF2 pathway. *Acta Biochim Biophys Sin* 2021, 53: 1009–1016
18. Shen X, Zhao X, He H, Zhao J, Wei Y, Chen Y, Han S, *et al.* Evolutionary conserved circular MEF2A RNAs regulate myogenic differentiation and skeletal muscle development. *PLoS Genet* 2023, 19: e1010923
19. Cilenti F, Barbiera G, Caronni N, Iodice D, Montaldo E, Barresi S, Lusito E, *et al.* A PGE2-MEF2A axis enables context-dependent control of inflammatory gene expression. *Immunity* 2021, 54: 1665–1682.e14
20. Galardi-Castilla M, Fernandez-Aguado I, Suarez T, Sastre L. Mef2A, a homologue of animal Mef2 transcription factors, regulates cell differentiation in Dictyostelium discoideum. *BMC Dev Biol* 2013, 13: 12
21. Ji X, Chen Z, Wang Q, Li B, Wei Y, Li Y, Lin J, *et al.* Sphingolipid metabolism controls mammalian heart regeneration. *Cell Metab* 2024, 36: 839–856.e8

22. Liu B, Pang L, Ji Y, Fang L, Tian CW, Chen J, Chen C, *et al.* MEF2A is the trigger of resveratrol exerting protection on vascular endothelial cell. *Front Cardiovasc Med* 2022, 8: 775392
23. Li H, Wang F, Guo X, Jiang Y. Decreased MEF2A expression regulated by its enhancer methylation inhibits autophagy and may play an important role in the progression of Alzheimer's disease. *Front Neurosci* 2021, 15: 682247
24. Wang L, Fan C, Topol SE, Topol EJ, Wang Q. Mutation of MEF2A in an inherited disorder with features of coronary artery disease. *Science* 2003, 302: 1578–1581
25. Xu DL, Tian HL, Cai WL, Zheng J, Gao M, Zhang MX, Zheng ZT, *et al.* Novel 6-bp deletion in MEF2A linked to premature coronary artery disease in a large Chinese family. *Mol Med Rep* 2016, 14: 649–654
26. Yu J, Yang Y, Xu Z, Lan C, Chen C, Li C, Chen Z, *et al.* Long Noncoding RNA *Ahit* protects against cardiac hypertrophy through SUZ12 (suppressor of zeste 12 protein homolog)-Mediated downregulation of MEF2A (myocyte enhancer factor 2A). *Circ Heart Fail* 2020, 13: e006525
27. Liu B, Wang L, Jiang W, Xiong Y, Pang L, Zhong Y, Zhang C, *et al.* Myocyte enhancer factor 2A delays vascular endothelial cell senescence by activating the PI3K/p-Akt/SIRT1 pathway. *Aging* 2019, 11: 3768–3784
28. Lee C, Huang CH. LASAGNA-Search: an integrated web tool for transcription factor binding site search and visualization. *BioTechniques* 2013, 54: 141–153
29. Singh CK, Chhabra G, Ndiaye MA, Garcia-Peterson LM, Mack NJ, Ahmad N. The role of sirtuins in antioxidant and redox signaling. *Antioxid Redox Signal* 2018, 28: 643–661
30. Di Minno A, Turnu L, Porro B, Squellerio I, Cavalca V, Tremoli E, Di Minno MND. 8-Hydroxy-2-deoxyguanosine levels and cardiovascular disease: a systematic review and meta-analysis of the literature. *Antioxid Redox Signal* 2016, 24: 548–555
31. Dubois-Deruy E, Peugnet V, Turkieh A, Pinet F. Oxidative stress in cardiovascular diseases. *Antioxidants* 2020, 9: 864
32. Li X, Zou J, Lin A, Chi J, Hao H, Chen H, Liu Z. Oxidative stress, endothelial dysfunction, and *N*-acetylcysteine in type 2 diabetes mellitus. *Antioxid Redox Signal* 2024, 40: 968–989
33. Liu B, Fang L, Mo P, Chen C, Ji Y, Pang L, Chen H, *et al.* Apoe-knockout induces strong vascular oxidative stress and significant changes in the gene expression profile related to the pathways implicated in redox, inflammation, and endothelial function. *Cell Signal* 2023, 108: 110696
34. Forman HJ, Zhang H. Targeting oxidative stress in disease: promise and limitations of antioxidant therapy. *Nat Rev Drug Discov* 2021, 20: 689–709
35. Peng X, Sun B, Tang C, Shi C, Xie X, Wang X, Jiang D, *et al.* HMOX1-LDHB interaction promotes ferroptosis by inducing mitochondrial dysfunction in foamy macrophages during advanced atherosclerosis. *Dev Cell* 2025, 60: 1070–1086.e8
36. Guo X, Kesimer M, Tolun G, Zheng X, Xu Q, Lu J, Sheehan JK, *et al.* The NAD+-dependent protein deacetylase activity of SIRT1 is regulated by its oligomeric status. *Sci Rep* 2012, 2: 640
37. Ministrini S, Puspitasari YM, Beer G, Liberale L, Montecucco F, Camici GG. Sirtuin 1 in endothelial dysfunction and cardiovascular aging. *Front Physiol* 2021, 12: 733696
38. Xiao W, Wang RS, Handy DE, Loscalzo J. NAD(H) and NADP(H) redox couples and cellular energy metabolism. *Antioxid Redox Signal* 2018, 28: 251–272
39. Shelbayeh OA, Arroum T, Morris S, Busch KB. PGC-1α is a master regulator of mitochondrial lifecycle and ROS stress response. *Antioxidants* 2023, 12: 1075
40. Chuang YC, Chen SD, Jou SB, Lin TK, Chen SF, Chen NC, Hsu CY. Sirtuin 1 regulates mitochondrial biogenesis and provides an endogenous neuroprotective mechanism against seizure-induced neuronal cell death in the hippocampus following status epilepticus. *Int J Mol Sci* 2019, 20: 3588
41. Batty M, Bennett MR, Yu E. The role of oxidative stress in atherosclerosis. *Cells* 2022, 11: 3843
42. Münzel T, Daiber A. Vascular redox signaling, endothelial nitric oxide synthase uncoupling, and endothelial dysfunction in the setting of transportation noise exposure or chronic treatment with organic nitrates. *Antioxid Redox Signal* 2023, 38: 1001–1021
43. Varghese MV, James J, Rafikova O, Rafikov R. Glucose-6-phosphate dehydrogenase deficiency contributes to metabolic abnormality and pulmonary hypertension. *Am J Physiol-Lung Cell Mol Physiol* 2021, 320: L508–L521
44. Bu X, Wu D, Lu X, Yang L, Xu X, Wang J, Tang J. Role of SIRT1/PGC-1&alpha in mitochondrial oxidative stress in autistic spectrum disorder. *Neuropsychiatr Dis Treat* 2017, Volume 13: 1633–1645
45. Liu J, Jiang J, Qiu J, Wang L, Zhuo J, Wang B, Sun D, *et al.* Urolithin A protects dopaminergic neurons in experimental models of Parkinson's disease by promoting mitochondrial biogenesis through the SIRT1/PGC-1α signaling pathway. *Food Funct* 2022, 13: 375–385
46. Cantó C, Menzies KJ, Auwerx J. NAD+ metabolism and the control of energy homeostasis: a balancing act between mitochondria and the nucleus. *Cell Metab* 2015, 22: 31–53
47. Imai S, Guarente L. NAD+ and sirtuins in aging and disease. *Trends Cell Biol* 2014, 24: 464–471
48. Li C, Sun XN, Chen BY, Zeng MR, Du LJ, Liu T, Gu HH, *et al.* Nuclear receptor corepressor 1 represses cardiac hypertrophy. *EMBO Mol Med* 2019, 11: e9127
49. Ikeda S, He A, Kong SW, Lu J, Bejar R, Bodyak N, Lee KH, *et al.* MicroRNA-1 negatively regulates expression of the hypertrophy-associated calmodulin and mef2a genes. *Mol Cell Biol* 2009, 29: 2193–2204
50. Shen Y, Zhang T, Jia X, Xi F, Jing W, Wang Y, Huang M, *et al.* MEF2A, a gene associated with mitochondrial biogenesis, promotes drug resistance in gastric cancer. *Biochim Biophys Acta Mol Basis Dis* 2025, 1871: 167497
51. Potthoff MJ, Olson EN. MEF2: a central regulator of diverse developmental programs. *Development* 2007, 134: 4131–4140
52. Xiong Y, Wang L, Jiang W, Pang L, Liu W, Li A, Zhong Y, *et al.* MEF2A alters the proliferation, inflammation-related gene expression profiles and its silencing induces cellular senescence in human coronary endothelial cells. *BMC Mol Biol* 2019, 20: 8
53. Li C, Fang F, Wang E, Yang H, Yang X, Wang Q, Si L, *et al.* Engineering extracellular vesicles derived from endothelial cells sheared by laminar flow for anti-atherosclerotic therapy through reprogramming macrophage. *Biomaterials* 2025, 314: 122832
54. Lu YW, Martino N, Gerlach BD, Lamar JM, Vincent PA, Adam AP, Schwarz JJ. MEF2 (myocyte enhancer factor 2) is essential for endothelial homeostasis and the atheroprotective gene expression program. *Arterioscler Thromb Vasc Biol* 2021, 41: 1105–1123
55. von Scheidt M, Zhao Y, Kurt Z, Pan C, Zeng L, Yang X, Schunkert H, *et al.* Applications and limitations of mouse models for understanding human atherosclerosis. *Cell Metab* 2017, 25: 248–261
56. Xie B, Lin J, Chen X, Zhou X, Zhang Y, Fan M, Xiang J, *et al.* CircXRN2 suppresses tumor progression driven by histone lactylation through activating the Hippo pathway in human bladder cancer. *Mol Cancer* 2023, 22: 151